


The Development of a Lanthanum Bromide Scintillation Detector for SPECT Imaging

Jonathan T. Sutton

College of William and Mary, Physics Department

April 30, 2008

Abstract

To improve the sensitivity, spatial and energy resolution available in Single Photon Emission Computed Tomography detectors, various components of a new design of gamma camera have been tested. A single piece of $LaBr_3$ has been coupled (Bicron-St Gobain Inc.) to four position sensitive photomultiplier tubes (PSPMT) to create a novel detector capable of *in vivo* biological imaging with significantly improved imaging capabilities. Specialized readout circuitry has been developed and implemented to reduce the number of active channels. In addition, an investigation into the possibility of a special algorithm capable of reconstructing SPECT images without pixellation has been completed. The development of this detector will be of special importance to collaborative studies at William and Mary. *Mus musculus* infected with the mouse mammary tumor virus (MMTV) express significant amounts of the sodium iodine symporter (Na^+/I^-) in proliferating tumor cells. The radiopharmaceutical Na-^{125}I can be injected into a mouse to track the distribution of the tracer throughout the animal using SPECT imaging. The new detector will improve the results of this biological study.

Work Supported by the U.S NIH Grant (EB000458-02), the U.S DOE, the U.S DOD Breast Cancer Research Program (BC046053), and a grant funded by the Howard Hughes Medical Institute Undergraduate Biological Sciences Education Program through the College of William and Mary.

Table of Contents

Figures

Tables

1. Introduction

1.1 Biomedical Imaging

Over recent decades, advances in various areas within the scientific community have significantly affected the field of biomedical imaging. As biomedical research continues to reveal the mechanisms behind the complexities of the human body, the demand has increased for high quality images of affected areas. The ability to image not only allows medical professionals to operate at a more efficient and adept pace, but also provides an increasingly advanced and direct route to new discoveries. Imaging modalities that have received special research attention include those devoted to observing a subject's function, such as functional magnetic resonance imaging (fMRI), positron emission tomography (PET), ultrasonic imaging (ultrasound), and single photon emission computed tomography (SPECT). These methods have also been successful in creating seamless images that are valuable in *in vivo* studies [5].

SPECT imaging is one example of a modality that has seen significant advances over past years. Using the radiation emitted from an injected pharmaceutical tracer, SPECT produces a two-dimensional image based on the distribution of tracer throughout a subject. Gamma photons directed toward the detector are first absorbed by an organic scintillator and re-emitted as visible light photons. These lower energy photons are absorbed and transformed by a photomultiplier tube into electrical signals, which are sent to a computer for image processing. By understanding the image distortions that each step in the process creates, effective software reconstruction programs have been developed to create a seamless image of a radiopharmaceutical distribution. Figure 1 shows a schematic of the imaging process and typical detector construction. SPECT also offers the possibility of 3-D imaging through the reconstruction of multiple planar images taken at different angular positions.

1.2 Challenges and Limitations

Various steps in the SPECT imaging process present challenges and limitations for developing systems. Radiation emitted from a radiopharmaceutical must first pass through biological tissue and air before reaching the detector. Those media possess different attenuation coefficients and will scatter the photons. Radiation passing through small amounts of skin tissue

tends to be minimally affected; however, internal studies involving attenuation by bone can significantly affect results. In addition, a great portion of the subjects analyzed in SPECT studies are model organisms which require anesthesia for proper studies. Anesthetics can significantly alter the metabolic processes of mammals and thus affect processes being studied. Weisenberger et. al. reported on a SPECT motion tracking system capable of tracking the motion of a mouse under little to no anesthetic. The researchers used infrared sensors to track six degrees of freedom of a dynamic radioactive phantom source [12]. These systems offer the possibility of eliminating the effects of the anesthetic on the subject animal. They are also examples of improvements in technology for the advancement of SPECT and similar biomedical imaging modalities.

1.3 Organization of Report

In recent years, similar advancements have been made in the manufacturing of high energy photon scintillation crystals and position sensitive photomultiplier tubes. This paper discusses the development of a $LaBr_3$ scintillation detector that utilizes some of the recent technological developments in these areas. Following complete construction, calibration, and testing, the detector will be implemented into the College of William and Mary biological imaging system to be used in a collaborative study by the Applied Science, Biology, and Physics departments. To assist in the testing and implementation stages, this paper address the following tasks: (1) provide a brief overview of the MMTV studies conducted at William and Mary using the current SPECT detectors, (2) describe and discuss the physical and structural components of the $LaBr_3$ detector as they have been tested thus far, and (3) discuss the implications of the development of this detector as they pertain to reconstructive algorithm software.

2. MMTV

In recent years, molecular biology research into gene expression has led to the need for high resolution imaging devices with the ability to observe biological processes *in vivo*. Collaborative studies at William and Mary use radioactive Na-^{125}I injected into an anesthetized mouse to effectively image the distribution of the radioactive molecule as it is distributed throughout the

animal's body. This selective distribution arises from the radioactive molecule's ability to bind to the Sodium Iodine symporter protein (NIS) and diffuse across the membrane of various cells. NIS is well known to be active in the thyroid gland, as it acts as the mediator of iodine uptake-- a requisite for effective biosynthesis of thyroid hormone.

2.1 NIS Expression

In addition to the thyroid gland, NIS has also been found to be expressed in other tissues. Figure 2 shows the distribution of NIS mRNA expression as found in various mouse tissues [11]. Most pertinent to the studies at William and Mary is NIS expression in the mouse mammary gland. NIS is found in the mammary gland at all stages of mouse development, but is most pronounced during the lactating stage. This is due to the need for a sufficient iodine intake in a newborn's diet. To provide an adequate source of I^- for the newborn, the level of NIS mRNA is upregulated in the mother's lactating breast. This results in increased translation of NIS protein and a rise in the level of I^- in the lactating breast [10].

NIS has also been shown to be expressed in proliferating cells affected with the Mouse Mammary Tumor Virus (MMTV). Figure 3 shows the immunohistochemistry results of a study done to test for the presence of NIS in tumors at different stages of development. In all of these tests, IHC consistently shows expression of the protein within the tumor. This can be compared to the region of interest (ROI) plot of the corresponding SPECT image [2]. This presence of NIS in a proliferating tumor coupled with Na-^{125}I's affinity to NIS provides an effective mechanism for *in vivo* imaging of a mouse mammary tumor.

2.2 Interpretation of Planar Images with NaI(Tl) SPECT Detector

The current detector in use at the William and Mary lab implements a NaI(Tl) pixilated scintillator with a 46 x 96 mm viewing area. Figure 4 shows the Na-^{125}I distribution in a mouse between 40 and 45 minutes after injection. Hot spots can be seen in the thyroid (top middle), stomach (bottom right), and mammary tumor (top left). The intensity of each pixel corresponds to the color scale found on the bottom right. Over 60 mice have been analyzed similarly for the uptake of Na-^{125}I and the results cataloged digitally. To properly interpret these images, a method to quantify the size, intensity, and distribution of ^{125}I was developed. This provides the ability to isolate any region of interest within the two-dimensional image and quantify the uptake

during the imaging process. Additionally, the pixel intensity in any part of the isolated region could be normalized to take into account the background uptake of ^{125}I. Any pixel with photon event counts above this threshold could be included and those with counts below this level set to zero. The result was an isolated region of interest that represented pixels with significant uptake activity which could be quantified and analyzed over time.

Figure 5 shows the progression of ^{125}I distribution in Mouse 248 from the time of injection until one hour in time cut increments. To observe the size progression of the tumor, the total number of pixels above a threshold, based on the accumulation of isotope in the animal's abdomen, was set and analyzed. The data show one conclusive characteristic: the correspondence between tumor size and ^{125}I distribution. In older mice with well-developed tumors, a great deal of heterogeneity can be seen in the SPECT images, whereas the newly developed tumors have a highly localized uptake of ^{125}I. Figures 5 and 7 can be compared to show the difference in pattern of uptake between two different size tumors in different stages of development.

The overall interpretation of this pattern is most likely the result of tumor necrosis. As a tumor progresses, coagulated blood builds up around the necrotic region disabling the binding of ^{125}I. Over 15 mice were analyzed using similar procedures; however the results pertaining to additional pattern interpretations have been inconclusive. Regardless, the current SPECT system is an effective way of examining mammary tumor development, and will only become more effective with detector parameter improvement.

3. SPECT Detector Construction

3.1 Radionuclides

SPECT detectors generally employ an organic scintillator to absorb ionizing radiation and produce visible light capable of generating a corresponding electronic signal. These scintillators are diverse in their energy ranges and must effectively absorb radiation from the radiopharmaceutical used in a particular study. Thus, selection of an appropriate radioactive tag is crucial. A variety of radioactive isotopes are used in SPECT and Positron Emission

Tomography (PET) studies. Table 1 shows some similar studies on functional imaging and isotope use.

Radiopharmaceuticals incorporate a radioactive isotope to allow for effective imaging. MMTV studies use a Na-^{125}I molecule that emits gamma and x-rays. The emitted 35 KeV gamma ray is of particular importance. At this energy, the photon readily passes through several millimeters of tissue but has a very high absorption coefficient in high Z materials such as lead or tungsten. Photon interaction with various media is described by Equation 1.

$$I(x) = I_0 e^{\mu \rho x} \tag{1}$$

where:

$I(x)$= radiation intensity

I_0 = initial intensity

μ = absorption coefficient cm^2 / g

ρ = density of material g / cm^3

x = path length

3.2 Collimators

Gamma photons are emitted from the radionuclide in all directions. To produce a useful image, a SPECT detector must select for those photons traveling perpendicular to the scintillating surface, just as a lens does for visible light. This is accomplished in SPECT imaging through the use of a collimator. Various types of collimators can be used; however, each has trade offs with sensitivity and resolution. Parallel-hole collimators consist of arrays of small holes constructed from high Z materials to absorb radiation not following a direct path. Pinhole collimators permit image magnification, but with relatively low sensitivity. They are generally used when only a small viewing area is required and higher spatial resolution is desired.

The resolution of a detector is highly dependent on the geometry of the collimator. The total system resolution is a factor of both the collimator resolution and the detector's intrinsic resolution. A schematic of this process using parallel-hole collimation can be seen in Figure 8 and theoretically obeys the following [13]:

$$R = L \frac{e + a + c}{e} \tag{2}$$

$$e = e' - \frac{2}{\mu} \tag{3}$$

where:

R = resolution of collimator

L = diameter of collimator holes

e = effective depth of collimator

e'= depth of collimator

b = distance between specimen and collimator

c = separation between collimator and scintillator

3.3 Scintillators

High energy photons passing through the collimator are converted to a lower energy that can more readily be detected and processed using a scintillator and photomultiplier tube. Scintillators can be constructed from organic or inorganic materials and their properties are highly dependent on their type. Organic materials offer very fast decay times, but have lower efficiencies than inorganic materials. Inorganic scintillators are generally used in imaging studies from their fast response time.

Two main types of scintillators have been used at William and Mary in the past: thallium-doped sodium iodide [NaI(Tl)] and sodium-doped cesium iodide [CsI(Na)]. Compounds are doped to achieve a faster, more efficient scintillation by decreasing the width of the band gap, reducing the amount of energy necessary to excite an electron to the conduction band. This also lowers the energy of the emitted photon to a detectable level in the UV to visible spectral range. Traditional scintillators for use in imaging studies have also been pixellated to aid in the spatial mapping process of image construction. Pixellation involves constructing the scintillator from an array of tiny, volumetric crystal of, for example, 1 x 1 x 5 mm.

Recently available as a scintillation material is cerium-doped lanthanum bromide [$LaBr_3$(Ce)]. This compound offers higher energy resolution, faster decay times, and improved sensitivity over traditional NaI(Tl) and CsI(Na) crystal scintillators. The detector currently being developed uses a monolithic slab of $LaBr_3$(Ce) crystal as its scintillation material and does not implement pixellation. Table 2 shows some properties of these scintillating materials.

3.4 Photomultiplier Tubes

The final stage of detection consists of scintillation light detection. This is done via position-sensitive photomultiplier tubes (PSPMT), which differ from traditional photomultiplier tubes from the substitution of segmented anode wire grid or anode pads for position detection.

PMTs consist of three main stages: a photocathode, dynode stages, and anode. The choice of a photocathode should match well with the scintillator in the emitting and absorbing wavelengths. In SPECT studies, a bi-alkali metal absorbs the faint scintillation signal and emits electrons. Once an electron is ejected from the photocathode, it is directed towards a series of dynodes, separated by increasing positive voltages. Each stage provides a secondary emission and a net gain of electrons and is formed in a manner as to retain the impinging photon's position. Over a series of stages, sufficient signal gains can be achieved that are a function of the scintillation light. Typical gains observed are in the range of 1.5 million electrons per photon. Much of SPECT imaging relies on the resolution provided by the PSPMT's segmented anode which provides an intrinsic sub-millimeter resolution. A wire grid collects the cloud of electrons and sends the electrical signal to an ADC. This is further discussed in the $LaBr_3$ detector section.

4. Imaging at William and Mary

4.1 Previous Work

Collaboration at William and Mary has resulted in the development of a number of scintillation detectors using both pinhole and parallel-hole collimation. Recently, these detectors have been used together and tested to perform multi-pinhole circular/helical SPECT imaging. This system has proven to exhibit sub-millimeter spatial resolution after image reconstruction using pinhole collimation. The detectors have used NaI(Tl) and CsI(Na) scintillation crystals and various types of PSPMTs. Using parallel-hole collimation, a resolution around 2 millimeters and a sensitivity around 2000 count/min/μCi has been achieved for sources very close to the detector. Data from a study conducted on the NaI(Tl) detector in 2005 can be seen in Figure 9.

4.2 A Lanthanum Bromide Detector

4.2.1 Design

The construction, calibration, and early testing stages of a $LaBr_3$ scintillation detector began in the summer of 2007 at the Thomas Jefferson National Detector and Imaging Lab. The detector has an active viewing area of 100 cm^2, nearly doubling the area of the previously

described detectors. This detector utilizes all the basic components described above. Two views can be seen in Figure 17.

Instead of the traditional pixilated scintillation crystal, a monolithic slab of $LaBr_3$ has been used. This method will increase the overall sensitivity of the detector by allowing the photons striking the entire area of the scintillator to be processed. Previously, some photons struck the regions between scintillators and thus, some information was lost.

In addition to improved sensitivity, the use of $LaBr_3$ offers improved energy resolution. This stems from the compound's increased light yield compared to NaI(Tl) and CsI(Na). PET studies using $LaBr_3$ have shown energy resolutions around 4.1% at 511 KeV, compared to similar studies of NaI(Tl) scintillators showing 7.5% at 35 KeV [6].

The photomultiplier component of the apparatus has also been improved. Recently the Hamamatsu Inc. H9500 PSPMT has become readily available. The H9500 is similar to the device described above, but implements an array of 16 x 16 anode pad channels (compared to 8 x 8 in the H8500 PSPMT). This should improve spatial resolution, by enabling each event to be described by channels spaced twice as close to one another.

4.2.2 Implications

To enhance the resolution and sensitivity of such a detector with these improved components, a number of complications must be resolved. By eliminating the scintillator pixellation, the mapping of an event occurring on the anode array to its required location on the image becomes more difficult. Additional details and work completed is discussed below.

Another problem that must be resolved arises from the use of four (4) PSPMTs each having arrays of 16 x 16 anode pads. Data acquisition from this setup requires 1024 channels, significantly slowing image processing. To reduce the number of active channels, additive readout circuitry has been implemented, allowing a matrix of anode channels to be combined and then resolved via voltage dividers.

Finally, NaI(Tl) and CsI(Na) have provided emission spectra with peaks at 420 and 415 nm respectively. This matches the excitation spectrum maximum (400 nm; Table 2) of the bi-alkali photocathode employed in the H9500 PSPMT (Figure 11). $LaBr_3$(Ce) emits with a peak at 380 nm. This is considerably different than previous scintillators and the effects of such a change should be studied.

4.2.3 Measurements

Initial work on calibration involved an attempt to resolve the scintillator locations along the fringes of each adjacent PSPMT. Using a lead collimating mask with evenly spaced drilling and a ^{60}Co radioactive flood source, a carefully spaced uniform array of photons were produced on the surface of the scintillator. This provided a control to make software uniformity corrections. Knowing the total number and exact spacing of the holes, adjustments to the anode software coefficient factors in the center of gravity calculation were attempted. This method provided some additional spacing at the PSPMT fringes and will assist in the complicated image reconstruction discussed later.

To calculate a rough estimate of the detector's spatial resolution capabilities, a stick figure mask was flooded with gamma ray sources of two different energies: 166 keV and 30 keV. The resulting images can be seen in Figure 12 along with the mask and its corresponding dimensions. The holes in the body of the high energy image can be resolved but not above the head, indicating a resolution around 0.8 mm at 166 keV. More pertinent to this study is the image at 30 keV, comparable to ^{125}I. Holes above the head and in the body are blurred but much clearer in the head region. At this point in testing, the resolution cannot be precisely determined but is likely to be greater than 0.8 mm from a source located very close to the detector.

The explanation for this difference in resolution with varying energies is two-fold: a higher energy gamma photon will produce a greater number of scintillation photons and thus, photoelectrons to be detected at the anode pads. Also having a slight effect is the depth of interaction in the scintillating material. Higher energy photons penetrate deeper into the crystal before scintillation light is produced. The lower energy γ-photons penetrate a lesser distance, forcing the lower energy scintillation photons to travel a greater scattering distance to the PSPMT.

5. A Reconstructive Algorithm

5.1 Current Research

Three main factors have effects resulting in image deformity for systems currently in use. Each stems from an inherent property of a component of the system and must be dealt with in SPECT studies. When scintillation compounds are doped, impurities are added. However, it becomes very difficult in the doping process to achieve spatial uniformity of the material. This process, mixed with the imperfect crystal structure of the original compound, can produce image aberrations. In addition to material imperfections, photo-optical effects reduce the precision of a gamma ray event incident on a scintillation material. Operating based on the photoelectric effect, position sensitive PMTs produce a cloud of electrons for each incident event over a number of dynode stages. The result is a cloud of electrons with a Gaussian-like distribution that describes each single photon event.

The scintillator and PSPMT must also be physically connected, requiring a coupling medium. In previously reported systems, optical grease was used. However, this also has the effect of reducing the precision of an event due to the change in refractive effects in different media. Figure 13 shows the effect of a glass coupling medium on a flood image [3].

The effect most degrading to image quality originates when photons strike the photocathode of the PMT. The surface of the negatively charged photocathode is coated with a bi-alkali compound chosen for its low work function and spectral response in the UV to visible range. Inconsistencies on the surface of the photocathode degrade the Gaussian electron-cloud distribution. These three effects can deform the image and are dealt with in various ways.

5.2 An Approach for Monolithic Crystal Scintillation

The reconstructive algorithm presented here is an iterative peak reclamation process that has been explored by researchers at the Embry-Riddle Aeronautical University. It consists of a linear series of five steps that produces an array of cells, each with a unique property, corresponding to an incident photon location on the scintillation material. A non-exhaustive discussion of these steps is described below and can be viewed as a diagram in Figure 3. The

steps are: (1) loading "raw" data, (2) filtering and noise reduction, (3) peak identification, (4) Voronoi diagram plot generation, and (5) relocation [7].

The first step in this process is the input of raw data. Scientific literature on this method has been based on a raw flood image from a source such as ^{60}Co to generate an array of gamma ray projections from pixilated scintillators. However, in the $LaBr_3$ detector, the regular spacing provided by a pixilated array of crystals is not available, requiring a manual process to establish a reference array for incident photons. This has been accomplished with a lead test mask, consisting of an array of carefully spaced holes, the use of which results in an array of gamma ray projections similar to pixilated flood images. Tests with this mask have been previously reported and can be seen in Figure 14.

The raw data are then filtered for noise reduction and peak enhancement. This involves an iterative technique along the rows of the raw array, at each step multiplying the row by a function based on that row's raw count values. This process allows for better distinction between peaks and valleys in each row.

The third and most intensive step is the location of the peaks within the filtered data, where only array elements above a certain threshold are considered. Iteration through the elements in each row distinguishes one peak from another by assigning each value a score based on its geometry in relation to each peak in question. After computational techniques to distinguish the peaks, manual interaction is required to edit the computed peaks due to the inefficiency of the process. The result of this step is a rectangular grid of peaks, each with a specific coordinate in two-dimensional space. From this array of peaks, a new diagram is created. Figure 15 shows an example of such a plot, called a Voronoi diagram. These plots have the property that each point within a certain polygon is closer to that polygon's reference point than it is to any other reference point within the plane. Equation 4 describes a Voronoi polygon. Easily produced in MATLAB, the diagram can be a function of a set of points (x, y, z) within a plane or 3-dimensional figure.

$$T_i = \{x \in R^2 \mid d(x, x_i) \leq d(x, x_j) \forall j = 1,...n\} \tag{4}$$

Event data are gathered from each lead mask hole to determine its corresponding Voronoi cell and thus enable each raw peak to be mapped to its "correct" location on the image. Voronoi

polygons with corresponding correction vectors can be generated with each new flood image. The total correction vector becomes a weighted area overlap with the previously generated plot [7]. An example of this can be seen in Figure 16. After the flood correction array is generated, it can be applied to any incident gamma event.

6. Future Directions

The future direction of SPECT imaging at William and Mary is promising. The anticipated improvement in spatial resolution, sensitivity, energy resolution, and active viewing area will significantly increase the detector's efficacy in biological investigations. Multiple specimens will be studied simultaneously with a smaller dose requirement for similar sensitivity. The increase in resolution will enable more sensitive studies of biological mechanisms. Sub-millimeter (0.8 mm) resolution allows data for a tumor of large size (1 x 1 cm) to be partitioned into over 150 informational bins. The current system, with its resolution around 2 mm provides only 25. This will also require more enhanced imaging software that is streamlined into the system. The ability to image a specimen and immediately perform a quantitative analysis will be necessary.

7. Conclusions

In the fall of 2008, a small vertical crack was noticed on the lanthanum bromide scintillator of the developing detector. It was sent back to Bicron-St. Gobain Inc. for replacement and repairs. Since the discovery of the compound, quantities of crystal have been grown for scintillation, geophysical, medical, and security purposes. However, there has been a difficulty growing large portions of the crystal over 100 cm^2. Menge et. al. cite the spatially heterogeneous expansion and cooling of the crystal as the reason for this difficulty [8]. These properties have resulted in a high incidence of cracking.

Work has been done in initially investigating the resolving capabilities of the detector. Special techniques have also been applied to software and hardware to improve uniformity

across the surface of the imaged viewing area as well as a reduction in the number of active channels. Since the detector malfunction, an investigation into the possibility of a new reconstructive algorithm has taken place. Given the current research in SPECT reconstruction, this will be an endeavor worth considerable time and effort once testing continues. Finally, an analysis and review of germane applications using this detector has been completed and discussed.

8. Acknowledgements

Over the past year, through my experiences in the William and Mary REU program and senior research, I have had the pleasure of learning from a number of different people. I would like to thank initially my thesis advisor, Dr. Welsh, for the opportunity to participate in such a fascinating project and for the allotted trust in completing various endeavors. Secondly, I would like to thank Applied Science graduate student, Jianguo Qian, for his guidance in understanding the workings of the entire project. This included programming, detector function, and applications to biology.

I also thank Dr Bradley of Applied Science, Dr. Saha of Biology, and the William and Mary collaborative team for their guidance and fluid explanations of the biological and logistical aspects of research that may not come as easy to Physics students. Finally, I thank Dr. Stan Majewski, Dr. Drew Weisenberger and their brilliant team at the Thomas Jefferson Lab Detector and Imaging Group for teaching me the technical side of detector development along with unwavering patience with such an amateur to the field.

9. References

[1] Amidror, Isaac (2002). Scattered data interpolation methods for electronic imaging systems: a survey. Journal of Electronic Imaging. 11 (2), 157 – 172.

[2] Eric Blue, Stephen Schworer, Jianguo Qian, Eric L. Bradley, Margaret S. Saha, and Robert E. Welsh. *In vivo imaging of mammary tumors using a MMTV murine model.* William and Mary Graduate Research Symposium. February 2008.

[3] Bonifazi C., A. Tartari, M. N Cinti, L. Naneti, R. Pellegrini, R. Pani. (2004). Description of the response in scintillation crystal arrays: analytical versus statistical approaches. 213 (2). 231 - 235.

[4] Bradley, Eric L. , Julie Cella, Stan Majewski, Vladimir Popov, Jianguo Qian, Margaret S. Saha, Andrew G. Weisenberger, and Robert E. Welsh. (2006). A Compact Gamma Camera for Biological Imaging. IEEE Transactions on Nuclear Science. 53 (1), 59-65.

[5] Committee on the Mathematics and Physics of Emerging Dynamic Biomedical Imaging. National Academy Press, Washington D.C 1996. Mathematics and Physics of Emerging Biomedical Imaging.

[6] Kuhn, A., S. Surti, J. S. Karp, P. S. Raby, K. S. Shah. Design of a Lanthanum Bromide Detector for Time of Flight PET. (2004). IEEE Transactions on Nuclear Science. Vol. 51: 2550 – 2557.

[7] Maisler, B. D., H. Liu, J.E. McKisson, Yishi Li, Eric Kvam. (2007). Computational Geometric Techniques Applied to Spatial Calibration for Gamma Camera Images. Embry Riddle Aeronautical University, Laboratory of Advanced Instrumentation Research. 1 (1), 1-4.

[8] Menge, P. R, G. Gautier, A. Iltis, C. Rozsa, V. Solovyev. Performance of large lanthanum bromide scintillators. (2007) Nuclear Instruments and Methods in Physics Research, Vol. 579, 6–10.

[9] B Perron, A-M Rodriguez, G Leblanc and T Pourcher. Cloning of the mouse sodium iodide symporter and its expression in the mammary gland and other tissues (2001). Journal of Endocrinology, Vol. 170 185-196.

[10] Daniel H.Y. Shen,1 Richard T. Kloos,2,3 Ernest L. Mazzaferri,2 and Sissy M. Jhiang 1,2 Sodium Iodide Symporter in Health and Disease (2001). Thyroid. Vol. 11: 5.
Mary Ann Liebert, Inc.

[11] U. H. Tazebay, I. L. Wapnir, O. Levy, O. Dohan, L. S. Zuckier, Q. H. Zhao, H. F. Deng, P. S. Amenta, S. Fineberg, R. G. Pestell, and N. Carrasco. The mammary gland iodide transporter is expressed during lactation and in breast cancer. Nat Med 6:871–878.

[12] G. Weisenberger, A. S. Gleason, J. Goddard, B. Kross, S. Majewski, S. R. Meikle, M. J. Paulus, M. Pomper, V. Popov, M. F. Smith, B. L. Welch, and R. Wojcik. Restraint-Free Small Animal SPECT Imaging System With Motion Tracking. IEEE Transactions on Nuclear Science, Vol. 52, 3: 638 – 644, 2005.

[13] Weisenberger, A. Gamma Ray Imaging Detector for Small Animal Research. William and Mary PhD Dissertation. 1998.

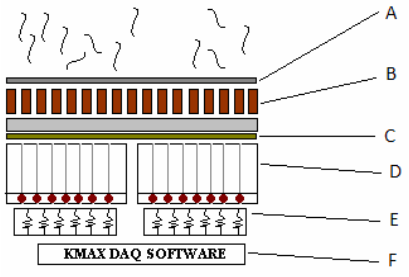

Figure 1. General detector components, (a) composite window (b) high Z parallel-hole collimator (c) scintillator coupling using optical glue (d) Position sensitive photomultiplier tubes (e)

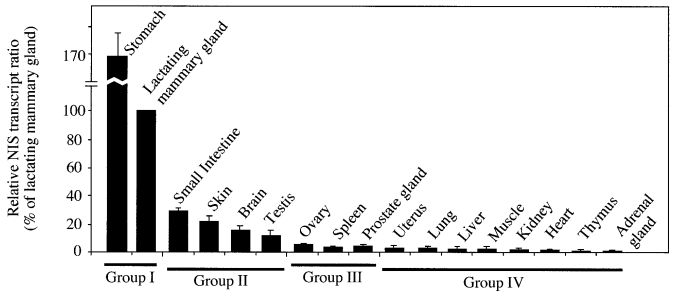

Figure 2 - NIS mRNA Distribution in various tissue of *Mus musculus*. Lactating mammary gland shows considerable expression. (Perron, 2001.)

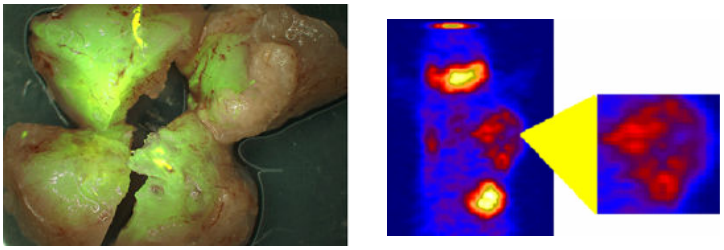

Figure 3,4. NIS Presence confirmed by whole-mount immunolocalization results. Tumor sectioned and shown to correlate with pattern of uptake from SPECT image. (Blue, 2007).

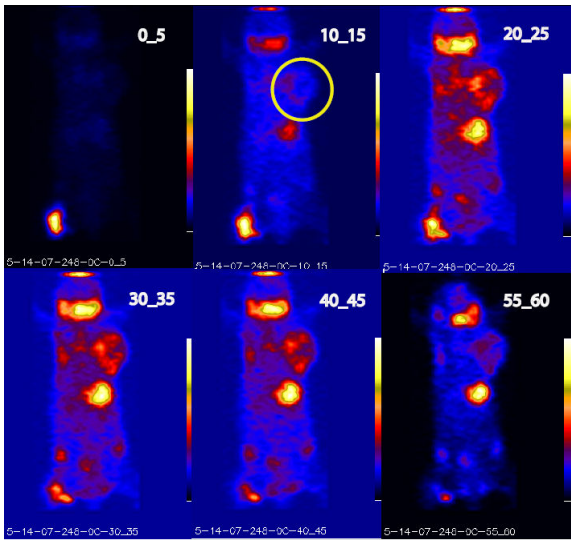

Figure 6. SPECT images of Na-^{125}I uptake distribution until one hour post-injection. Necrotic portions of tumor indicated by heterogeneous uptake pattern.

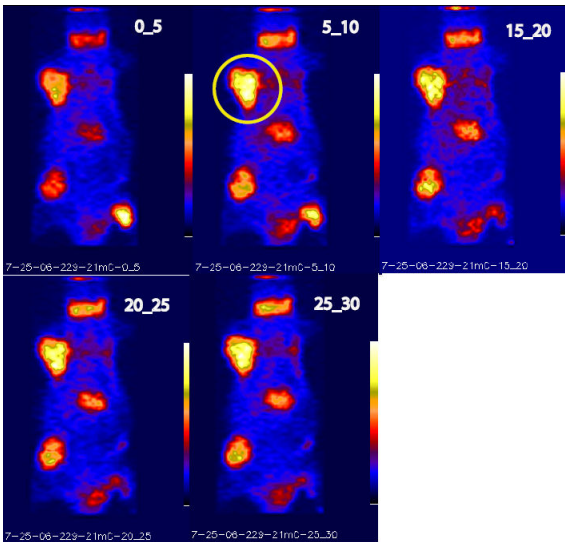

Figure 7. SPECT images of Na-^{125}I uptake distribution until 30 minutes post-injection. Encircled tumor consistent in isotope uptake; necrosis not evident.

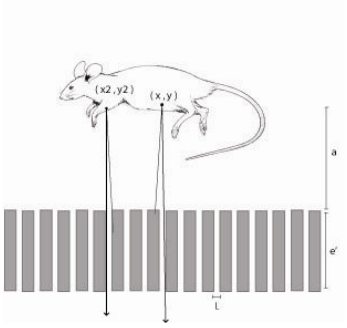

Figure 8. A schematic of parallel-hole collimation. Variable distances from collimator to specimen result in variable resolutions.

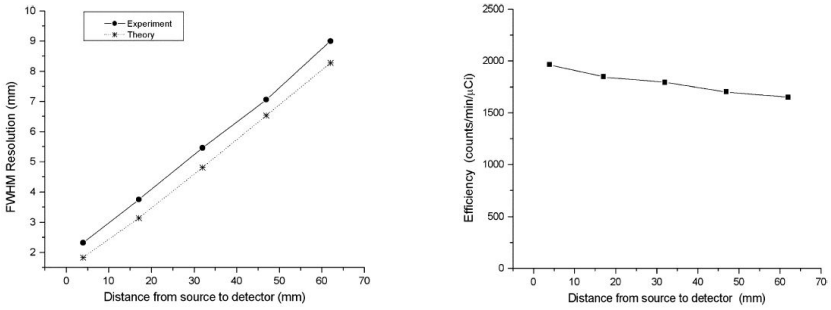

Figure 9. NaI(Tl) Detector Performance Data. Maximum resolution of 2 mm for typical studies close to detector (Qian, 2006).

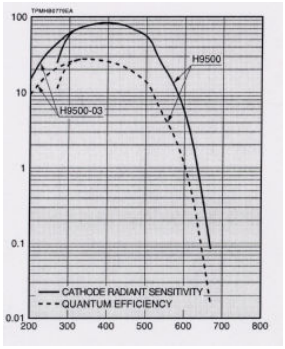

Figure 11. Spectral Response from Bi-Alkali Photocathode. $LaBr_3$ emission peak: 480 nm.

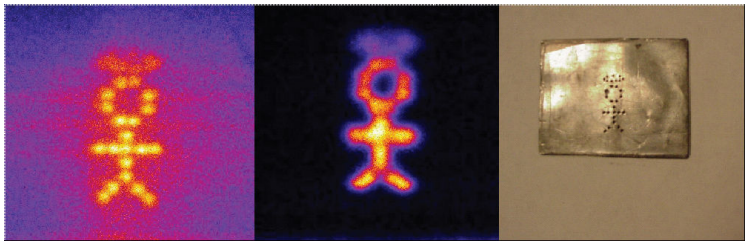

Figure 12. A rough estimation test. (Left) 166keV (Center) 30keV (Right) Lead Mask: Halo holes, 0.65mm; head and body holes, 0.8mm.

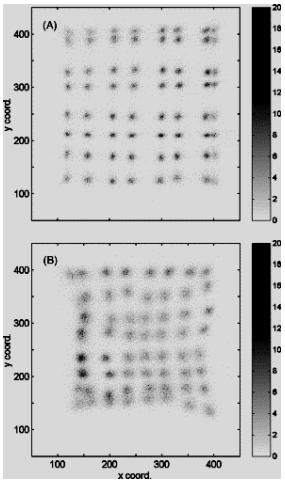

Figure 13. A regularly spaced collimator is used to show the effect of a glass coupling medium on image conformity. Refractive effects from the amorphic structure of the glass produce aberrations. (Bonifazi

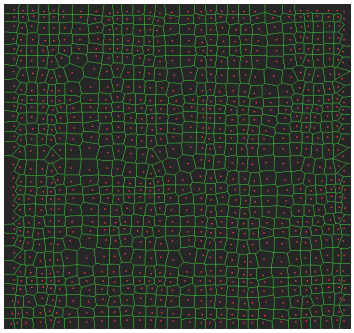

Figure 14. A Voronoi plot. Reference points in adjacent cells satisfy Equation 1.

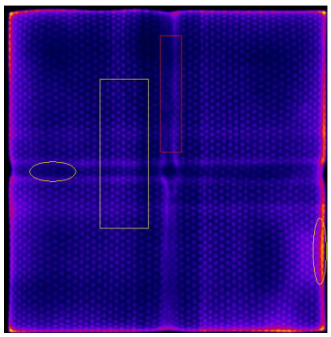

Figure 15. Raw Image using Pb mask. Holes between adjacent PSPMTs have been shifted from refractive effects.

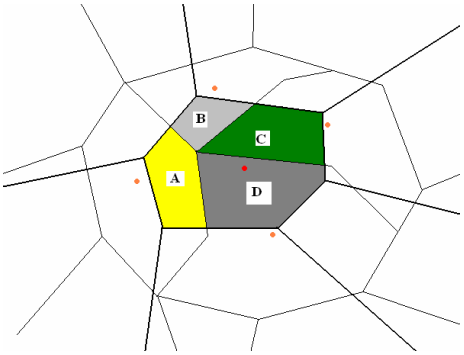

Figure 16. The generation of a correction vector. Photon locations from original flood are seen in background. Photon events(foreground) from second flood assume correction vectors as linear combination of overlapping Voronoi cells.

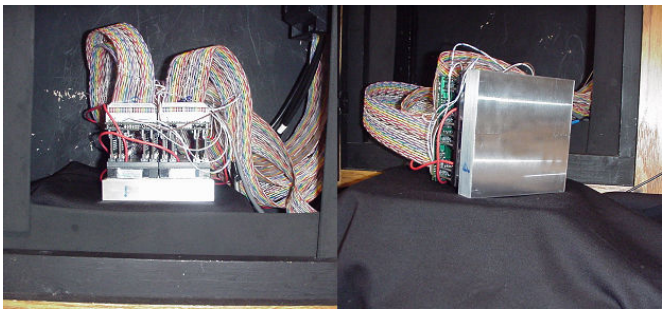

Figure 17. The $LaBr_3$ detector as seen in testing stage. (Right) The monolithic slab of Lanthanum Bromide as a scintillation material. (Left) Four Hamamatsu H9500 PSPMTs with readout circuitry.

Isotope	Application	Particle	Energy	Half Life
^{64}Cu	PET	e+	1.68 MeV	12.7 h
^{99m}Tc	SPECT	γ	140 KeV	6.01 h
^{125}I	SPECT	γ	35 KeV	60.2 d
^{60}Co	SPECT	γ	1.3 MeV	5.27 y

Table 1. Studies implementing radiopharmaceuticals

Scintillation Material	CsI(Na)	NaI(Tl)	$LaBr_3$(Ce)
Relative Light Yield	53.1	62.5	100
Density (g/cm^3)	4.51	3.67	5.06
Emission Maximum (nm)	420	415	380
Decay Time (μs)	630	230	0.02
Energy Resolution		7.5% (662 KeV)	4.1% (511 KeV)

Table 2. Properties of scintillation materials used in SPECT studies